A Numerical Experiment on Stochastic Condensation Theory

TERRY L. CLARK AND W. D. HALL

National Center for Atmospheric Research,[1] Boulder, CO 80307

(Manuscript received 30 August 1978, in final form 20 November 1978)

ABSTRACT

A three-dimensional numerical model is used to study the effect of small-scale supersaturation fluctuations on the evolving droplet distribution in the first 150 m above cloud base. The primary purpose of this research is to determine whether the irreversible coupling between the thermodynamics and dynamics due to finite phase relaxation time scales τ_S is sufficient to produce significant small-scale horizontal variations in supersaturation. Thus, the paper is concerned only with this internal source for thermodynamic variability. All other source terms, such as the downgradient flux of the variance of thermodynamic fields, have purposely been neglected.

Lagrangian particle experiments were run in parallel with the basic Eulerian model. The purpose of these experiments is to relax some of the microphysical parameterization assumptions with respect to assumed distribution shape and as a result add credibility to the results of distribution broadening.

Model results of five cases are presented, representing the cloud condensation nuclei characteristics of typical continental and maritime cumulus with mean dissipation rate of -100 cm^2 s^{-3}. The results show that for a maritime case of $N \approx 100$ cm^{-3} and $\bar{w} = 0.5$ m s^{-1} the standard deviation of the supersaturation is as large as its horizontal mean. The horizontal variability of all thermodynamic fields is shown to increase significantly with τ_S. The droplet broadening response to this irreversible coupling effect is found to be significant for the larger values of τ_S in the Eulerian experiments. The Lagrangian particle experiments showed a somewhat reduced but still significant effect.

Although the experiments do show a broadening effect caused by finite values of τ_S, in no case were we able to show a continual increase in distribution broadening with height as reported from cumulus observations.

1. Introduction

Cloud droplet size distributions have long been of interest to cloud physicists studying basic microphysical processes in clouds. A fundamental problem that has persisted over the years is to theoretically account for the observed broadness of the cloud droplet distribution during the early stages of growth before the processes of collision and coalescence take place. Early numerical experiments on the growth of a population of droplets by condensation theory (Howell, 1949; Squires, 1952; Mordy, 1959; Neiburger and Chien, 1960) were able to show that both the vertical velocity and cloud condensation nuclei (CCN) characteristics are important in determining the droplet population characteristics $\sim$100 m above cloud base. In all these cases the calculated droplet distributions were significantly narrower than those observed. Besides being narrower than observations, a structural difference of the calculated distributions was the almost complete absence of small numbers of droplets very much smaller and very much larger than the mean radius. It was pointed out by Howell (1949) that this early approach is incomplete and that evaporation in clouds was not fully studied.

The observational evidence of size distributions in cumulus clouds has been presented by Warner (1969a). In this paper Warner reports that cloud droplet distributions often have a bimodal structure with the frequency of this bimodal structure increasing with decreasing stability and distance from the cloud base.

Theoretical studies by Sedunov (1965) and Belyaev (1967) suggested that turbulent mixing may be responsible for creating the broad observed droplet spectra. The primary concern of these papers was the effect of fluctuating supersaturations and its effect on the evolving spectra. Due to the nonlinearity and general complexity of the problem, simplifying assumptions were made. Two assumptions made which relate to the present work are (i) that the phase relaxation time scale τ_S was assumed constant; and (ii) that supersaturation fluctuations S' were directly proportional to vertical velocity fluctuations w'. Both of these assumptions will be relaxed in the present work.

Numerical experiments of Warner (1969b) and Bartlett and Jonas (1972) attempted to simulate the effects of "turbulent mixing" by applying a highly

[1] The National Center for Atmospheric Research is sponsored by the National Science Foundation.

0022-4928/79/030470-14$07.50

time-dependent w to a Lagrangian parcel calculation of condensation growth. As pointed out by Clark (1974a) and Stepanov (1975), these experiments were deficient in that they neglect to account for any spatial correlations between thermodynamic and/or population characteristics and as a result neglect the essence of the problem. These experiments failed to find any broadening effect.

In order to avoid some of the pitfalls of the Lagrangian parcel calculation, we chose to simulate the stochastic nature of condensation in a three-dimensional numerical model framework. The domain of calculation is taken as a 200 m cube in the cloud-base region. A mean vertical velocity $\bar{w}$ is applied such that the time mean condensation level is $\sim$50 m into the domain. Effects of external forcing are confined to random forcing on V in the first two wavenumbers. This choice of forcing avoids any downgradient flux of thermodynamic variance. Thus, we have confined the problem to a study of the effect of internal sources of thermodynamic variability on evolving population characteristics. The fluctuating velocities on the smaller scales are supplied by a nonlinear transfer downscale from the randomly forced large-scale perturbations of u', v' and w'. A finite phase-relaxation time scale of the supersaturation field due to the droplet population allows for an irreversible coupling which in turn allows w' to generate fluctuations in the thermodynamic variables. It is only the effect of this irreversible coupling that this paper addresses. The intention of this approach is to be able to study one simpler aspect of this rather complex problem. Choosing to study the cloud base region has introduced the complexity of a strong verticle structure to the phase relaxation time scale τ_S.

In the current framework, there are three primary variables which define the regime of response. First, there is the dissipation rate ϵ which is prescribed as -100 cm^2 s^{-3} and determined by the rate of large-scale random forcing. This is a typical value of turbulent dissipation rate in cumulus clouds (MacPherson and Isaac, 1977). Second, there is the phase relaxation time scale, τ_S, which is determined by the cloud microphysical characteristics through the specification of the CCN spectra and w. Third, there is the mean Lagrangian time scale, $\tau_L(=L/\bar{w})$, where L is some arbitrary vertical length scale $\sim$100 m. Kabanov *et al.* (1971) combined ϵ and τ_S to form a phase relaxation length scale $L_S(\equiv\epsilon^{\frac{1}{2}}\tau_S^{\frac{3}{2}})$, where it was assumed that inhomogeneities on scales $>L_S$ can appreciably influence the drop spectra. In the numerical experiments to be presented L_S varies from $\sim$20 m very near cloud base to values $\sim$0.1 m about 150 m above cloud base. To properly access the influence of horizontal inhomogeneities produced by the irreversible coupling between the microphysics and thermodynamics it would seem appropriate to numerically resolve scales $\sim L_S$. Unfortunately it is difficult to both resolve L_S over a cloud depth of, say 100 m, and at the same time use physically reasonable values of ϵ, $\bar{w}$ and/or CCN concentration. As a result of this difficulty the present experiments have grid scales $\sim L_S$ in only a few grid points above the main nucleation zone with the chosen numerical grid scales of 10 and 6.67 m. Thus, with this low resolution the results of these experiments should be considered preliminary.

The results from numerical experiments on a problem as complex and sensitive as the present one require very careful analysis to insure that effects are due to the assumed physics rather than the numerical methods employed and/or parameterizations assumed. Since during the experiments it proved difficult to assess such artificial effects, each experiment is supplemented with an embedded kinematical Lagrangian particle experiment, i.e., a group of either 400 or 900 particles representing cloud droplets were advected through the integration domain using the local winds. The cloud-droplet radii were allowed to vary according to the diffusional growth equation for a dilute droplet and the local supersaturation. Since the broadening effects of a finite time scale for nucleation are neglected and the processes of local mixing are not explicitly included for these Lagrangian particle calculations, the results of the analysis of these spectra may be considered a *lower bound* for this type of calculation. The results of the Lagrangian particle experiment represent an averaging over the entire horizontal domain, i.e., a 200 m square.

As will become clear from later sections, these experiments represent a preliminary stage of development for this project. The resolution of the model is still rather low and some of the results are still in need of better theoretical explanation. The domain covered in ϵ, τ_S, τ_L parameter space is quite limited.

2. Model framework

a. Basic equations

The momentum equations for the moist air are represented in tensor form as

$$\bar{\rho}\frac{d}{dt}u_i=-\frac{\partial P'}{\partial x_i}+\delta_{i3}\bar{\rho}g(\theta^*+0.608q_v-q_l)+\frac{\partial}{\partial x_k}\tau_{ik}, \qquad (2.1)$$

where u_i, for $i=1, 2, 3$, represents the air velocity in the x, y and z directions, respectively. $\bar{\rho}$ and P' represent the environmental air density and perturbation pressure, respectively. The basic form chosen for the perturbation equations is the shallow anelastic equations of Ogura and Phillips (1962). In this framework $\bar{\rho}$ is taken as constant. θ^*, q_v and q_l represent the non-dimensionalized perturbation potential temperature, water vapor mixing ratio and liquid water mixing ratio.

The structures of θ and q_v are partitioned such that

$$\theta=\theta_0+\theta'(z)+\theta''(\mathbf{x},t)=\theta_0(1+\theta^*), \tag{2.2}$$

$$q_v=q_v'(z)+q_v''(\mathbf{x},t), \tag{2.3}$$

where horizontal averages of $\overline{\theta''}^{xy}=\overline{q_v''}^{xy}=0$. These formulations will be used later to describe the model's boundary conditions. The stress tensor τ_{ij} is taken as proportional to the deformation tensor D_{ij} according to the first-order theory of Smagorinsky (1963) and Lilly (1962) where

$$\tau_{ij}=\bar{\rho}K_M D_{ij} \tag{2.4}$$

and K_M is the eddy mixing coefficient. D_{ij} and K_M are taken as

$$D_{ij}=\frac{\partial u_i}{\partial x_j}+\frac{\partial u_j}{\partial x_i}-\frac{2}{3}\delta_{ij}\frac{\partial u_k}{\partial x_k}, \tag{2.5}$$

$$K_M=\frac{(C\Delta)^2}{\sqrt{2}}|\mathrm{Def}|, \tag{2.6}$$

where the three-dimensional total deformation is given as

$$\mathrm{Def}^2=D_{11}^2+D_{22}^2+D_{33}^2+\tfrac{1}{2}(D_{12}^2+D_{23}^2+D_{13}^2). \tag{2.7}$$

In Eq. (2.6) $C=0.3$ and $\Delta=(\Delta x\Delta y\Delta z)^{\frac{1}{3}}$ were chosen. Considering Deardorff (1971) a somewhat smaller value of C may have been more appropriate.

The shallow "anelastic" equations of Ogura and Phillips (1962) reduce the mass continuity equation for dry air to

$$\frac{\partial u_k}{\partial x_k}=0 \tag{2.8}$$

since $\bar{\rho}$ is taken as a constant and the anelastic approximation assumes the local time derivative of ρ is to be neglected.

The equations for θ^*, q_v and q_1 are treated using the equations

$$\frac{d}{dt}\theta^*=\frac{LC_d}{C_p\bar{T}}+\frac{\partial}{\partial x_k}\left(K_M\frac{\partial\theta^*}{\partial x_k}\right), \tag{2.9}$$

$$\frac{d}{dt}q_v=-C_d+\frac{\partial}{\partial x_k}\left(K_M\frac{\partial q_v}{\partial x_k}\right), \tag{2.10}$$

$$\frac{d}{dt}q_1=+C_d+\frac{\partial}{\partial x_k}\left(K_M\frac{\partial q_1}{\partial x_k}\right), \tag{2.11}$$

where an eddy Prandtl number of unity has been assumed. L and C_p are the latent heat of vaporization and specific heat at constant pressure, respectively. Careful treatment of the coupling between the dynamics, thermodynamics and microphysics must be considered. The coupling exists through the condensation rate C_d, where in general terms

$$C_d=4\pi\frac{\rho_w}{\rho}\int_0^\infty r^2 f(r)\frac{dr}{dt}\delta r, \tag{2.12}$$

where $f(r)$ is the density function describing the number of droplets between radii r to $r+\delta r$ per cubic centimeter of air and dr/dt is the diffusional growth rate of a droplet of radius r. Any treatment given to the microphysics must give a reasonable treatment to (2.12) such that the relevant feedback mechanisms between supersaturation, vertical velocity and droplet population characteristics are properly maintained.

b. *Microphysical parameterization*

The treatment chosen for the droplet population microphysics uses a single lognormal distribution function. This parameterization is taken from Clark (1979) and will be only briefly described in this paper. We start with the kinematic equation

$$\frac{df}{dt}(r)=-\frac{\partial}{\partial r}\left[f(r)\frac{dr}{dt}\right]+\frac{\partial}{\partial x_k}\left[K_M\frac{\partial f}{\partial x_k}(r)\right], \tag{2.13}$$

where again we have chosen identical subgrid-scale closure for $f(r)$ as used for the basic thermodynamic variables. The first term on the right-hand side of (2.13) represents the diffusional growth of the droplet population by condensation. Note that if we multiply (2.13) by r^3, integrate from $r=0$ to ∞ and multiply the result by an appropriate constant we will have identically reproduced Eqs. (2.11) and (2.12).

The next step in the parameterization is to approximate $f(r)$ as a single lognormal distribution function

$$f(\ln r)=\frac{N}{\sqrt{2\pi}\sigma}\exp[-(\ln r-\mu)^2/2\sigma^2], \tag{2.14}$$

where N, μ and σ are the total number concentration of droplets per cubic centimeter of air, the logarithmic mean and logarithmic standard deviation, respectively. Without a subscript, σ will refer to logarithmic standard deviation throughout the text, whereas with a subscript (e.g., σ_ϕ), σ will refer to the standard deviation of ϕ. In order to consider advection, eddy mixing and droplet diffusional growth we need three equations for the three basic field variables of N, μ and σ. Advection and diffusion are treated separately from the diffusional droplet growth. This type of treatment has been the rule in cloud modeling for many years now, e.g. Takeda (1971), Arnason and Greenfield (1972), Clark (1973), Soong (1974). Two choices are clear for the treatment of advection and diffusion. These are the parameters q_1 as in (2.11) without the C_d term and N, where from (2.13)

we derive

$$\frac{dN}{dt}=\frac{\partial}{\partial x_k}\left(K_M\frac{\partial N}{\partial x_k}\right). \tag{2.15}$$

Both q_1 and N are of such physical importance that it seems mandatory to treat them in a conservative manner in the model. The third parameter chosen for advection and diffusion of the droplet spectra is $N\mu$, where the advection equation is derived by multiplying (2.13) by $\ln r$ and integrating from $r=0$ to ∞. The result is

$$\frac{d}{dt}N\mu=\frac{\partial}{\partial x_k}\left(K_M\frac{\partial N\mu}{\partial x_k}\right). \tag{2.16}$$

Thus, Eqs. (2.11), (2.15) and (2.16) are used during the advection and mixing stage of treatment. At each grid point the distribution function is reconstructed using the three parameters N, $N\mu$ and q_1. This type of parameter choice for advection is similar to that used by Clark (1974b) where a Gamma distribution parameterization was applied to a two-dimensional problem except in that case N, $\bar{R}$ and q_1 were the chosen field variables.

The diffusional growth of droplets is treated by fitting the tendencies of the distribution parameters, $(d/dt)N$, $d\mu/dt$ and $d\sigma^2/dt$ to the predicted tendencies of the power moments d/dt (N, $N\overline{R^3}$ and $N\overline{R^6}$) derived using only the first term on the right-hand side of (2.13), where the power moment $N\overline{R^P}$ is defined as

$$N\overline{R^P}=\int_0^\infty r^P f(r)dr=N\exp[P\mu+P^2\sigma^2/2]. \tag{2.17}$$

The diffusional growth rate of droplets is approximated as

$$\frac{dr}{dt}=\frac{kS}{r+l}, \tag{2.18}$$

where curvature and solute effects have been neglected. The parameter k ($=0.98\ \mu m^2\ s^{-1}$ percent^{-1}) is a slowly varying thermodynamic parameter which has been taken as constant for these experiments. A small condensation coefficient was chosen which results in $l=2\ \mu m$ (e.g., Chodes *et al.*, 1974). The supersaturation S is defined as

$$S=q_v/q_{v_s}-1, \tag{2.19}$$

where q_{v_s} is the saturation value of q_v. Combining (2.13) and (2.18) we can derive a series approximation for the logarithmic power moment tendencies

$$\frac{d}{dt}\ln N\overline{R^P}=pkS\exp[-2\mu+2(1-P)\sigma^2]\alpha\left\{1+\beta(\beta-1)\times\sum_{n=1}^{4}\frac{(\alpha^2\sigma^2/2)^n}{n!}C_n\right\}, \tag{2.20}$$

where

$$\beta=l/r_0,$$
$$r_0=\exp[\mu+(P-2)\sigma^2],$$
$$\alpha=1/(1+\beta),$$
$$C_1=1,$$
$$C_2=\beta^2-10\beta+1,$$
$$C_3=\beta^4-56\beta^3+246\beta^2-56\beta+1,$$
$$C_4=\beta^6-246\beta^5+4047\beta^4-11\,572\beta^3+4047\beta^2-246\beta+1.$$

Choosing $P=0$, 3, 6 in (2.20) and equating the resulting three equations to the logarithmic tendency of the log-normal distribution

$$\frac{d}{dt}\ln N\overline{R^P}=\frac{d}{dt}\ln N+P\frac{d\mu}{dt}+\frac{P^2}{2}\frac{d\sigma^2}{dt}, \tag{2.21}$$

we are able to derive predictive equations for N, μ and σ^2. In order to apply these predictive equations, we also require a treatment of the supersaturation over the respective time interval. The quasi-analytical approach of Clark (1973) is used to treat S. This approach involves using a locally consistent supersaturation equation of the form (Squires, 1952)

$$\frac{dS}{dt}=T_S-H_2C_d\approx H_1w-S/\tau_S, \tag{2.22}$$

where T_S is the dynamic forcing due to adiabatic cooling of the rising air and H_2C_d is the opposing microphysical tendency due to the growth of existing droplets. The various terms in (2.22) are taken as

$$H_1=q_vg/(q_{v_s}R_d\bar{T})\cdot[R_dL(1-\theta^*)/(R_vC_p\bar{T})-1],$$
$$H_2=[1+q_vL^2/(R_vC_p\bar{T}^2)]/q_{v_s}, \tag{2.23}$$

where

$$\tau_S\alpha 1/(N\bar{R}).$$

In deriving q_{v_s}, the Clausius-Clapeyron equation

$$e_S=e_0\exp\left[\frac{L}{R_vT}\frac{(T-T_0)}{T_0}\right] \tag{2.24}$$

was chosen, which is consistent with the assumption of constant L. In the numerical treatment of (2.22) T_S is derived in a manner consistent with (2.9), (2.10) and (2.24).

A concept worth discussing at this time is the physical meaning of τ_S. The parameter τ_S represents the e-folding time for S to return to some quasi-equilibrium value. This quasi-equilibrium is found from (2.22) by putting $(d/dt)S\approx 0$ which results in

$$S_q=\tau_SH_1w. \tag{2.25}$$

The so-called "bulk-physical" models assume $\tau_S=0$ which in cloudy air results in 100% relative humidity

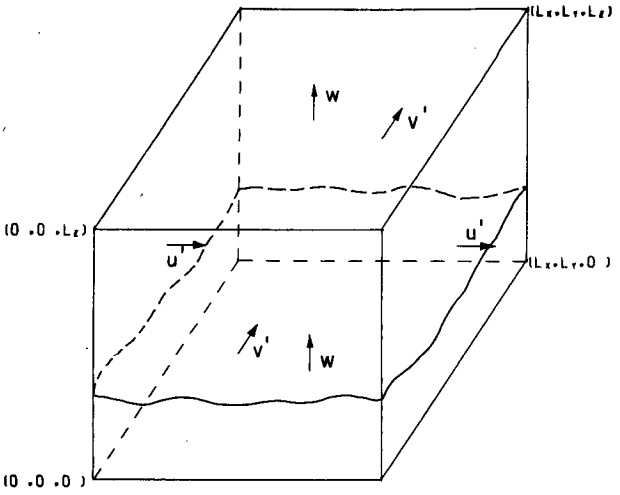

FIG. 1. Domain of integration. $L_x=L_y=L_z=200$ m. Subcloud region typically extends from $z=0$–50 m. Dry subcloud air is forced through the domain with a mean vertical velocity $\bar{w}$. Perturbation velocities u', v' and w' with zero horizontal averages are dynamically imposed on the flow.

or results in $S=S_q=0$. Thus, considering (2.23) our current model reduces in the limit to the "bulk-physical" model as $N\bar{R}\rightarrow\infty$.

Nucleation of CCN is treated in a rather simple manner where we assume a cumulative number concentration of small nuclei η which can be activated as

$$\eta=\mathrm{CCl}\,S_C^{0.5}, \tag{2.26}$$

where the critical supersaturation S_C is in percent supersaturation. The parameter CCl represents one of the main "tunable" constants of the experiments to be presented. Thus in our overall treatment of condensation and nucleation we first estimate the maximum level of S and check to see if current values of S exceed previously experienced values of S_C by comparing whether $N\lessgtr\eta$. If $N>\eta$ then nucleation is not considered but is $N<\eta$ then activated droplets are added to the distribution function such that $N=\eta$. When adding activated droplets, the distribution is shifted and possibly broadened to insure that neither $N\overline{R^3}$ nor $N\overline{R^6}$ is increased. This procedure avoids large instantaneous gains in either $N\overline{R^3}$ or $N\overline{R^6}$ due to nucleation. After droplets are added through nucleation the diffusional growth on existing droplets is treated through Eqs. (2.19)–(2.24).

One of the obvious weaknesses of this parameterized microphysics is that an assumed log-normal structure is strictly imposed on $f(r)$. This may at first be considered a rather serious imposition considering the main point of this research deals with effects of mixing on population breadth. This type of parameterization has previously been shown by Clark (1974a, 1974b) to produce accurate predictions of $N\bar{R}$. Having captured $N\bar{R}$ and, consequently, τ_S the overall coupling between the dynamics, thermodynamics and S is also reasonably well represented. In order to test the physical representativeness of the microphysical parameterization predictions of such parameters as the droplet distribution's coefficient of dispersion as well as deviations in structure from the lognormal distribution, we have also performed a set of non-interacting Lagrangian particle experiments. A set of particles of sufficiently small initial radii is released below cloud base, advected and allowed to grow/evaporate according to the numerical model's velocity and supersaturation conditions. Distribution functions are then constructed at prescribed height levels using the history of $\mathbf{x}$ and r for each of these particles. As discussed earlier this procedure has been used to supplement the parameterization results by supplying a lower bound estimate on the broadening effects of the irreversible coupling. Since all particles are initialized at the same radii ($r_0\sim0.1\ \mu$m) one could conceivably end up with Dirac delta functions at various vertical levels if indeed only the vertical excursion distance was important and history was negligible.

3. Boundary and initial conditions

Fig. 1 displays the physical domain of the model calculations. Dry subcloud air is forced through the domain with the mean vertical velocity $\bar{w}$. Deviations from $\bar{w}$ are produced by dynamically forcing $\mathbf{V}$ in the first two wavenumbers. This forcing produces a ragged cloud base at a height of $\sim$50 m from the $z=0$ inflow level. The boundary conditions imposed in the horizontal are x-y cyclic for all variables. In the vertical direction the boundary conditions are taken as

$$u',v',w',\theta'',q_v'' \text{ cyclic in } z. \tag{3.1}$$

At $z=0$, N, μ and σ are specified to equal threshold values N_0, μ_0 and σ_0, where the values

$$\mu_0=0.0018,\quad \sigma_0=0.06, \tag{3.2}$$

were chosen for all experiments. N_0 was chosen to be approximately one-quarter of its final upper level values. At the upper boundary of the cube $z=L_z$ one-sided differencing is used on the cloud physical variables if the region is locally an outflow region, i.e., if $w>0$. Local inflow regions are treated by applying the boundary condition

$$\frac{\partial}{\partial z}(N,N\mu,q_l)=0 \quad \text{at} \quad z=L_z \tag{3.3}$$

if $w<0$.

At initial time all microphysical variables are set equal to their respective threshold values. The thermodynamic variables are set equal to vertical profile values which allow the lifting condensation level to occur at $z=50$ m. q_v is reduced above the LCL such that $S=0$. Since the cyclic boundary conditions on q_v and θ^* are applied only to their deviations from their respective

horizontal averages, the mean level of the LCL remains constant throughout the model integration time.

4. Numerical methods

The basic numerical framework is taken from a simplified version of the three-dimensional model of Clark (1977). The model employs the second-order finite difference methods of Arakawa (1966) in the spatial dimensions and uses the second-order leapfrog scheme for the temporal treatment of $\mathbf{V}$, θ^* and q_v. The basic numerical approach used for advecting and mixing the microphysical field variables, N, $N\mu$ and q_1 is the second-order conservative scheme of Crowley (1968). Since this scheme does not assure positive definiteness of these fields a nonlinear "switch" was added through a modification of K_M such that where extreme gradients occur, as in the nucleation region, the scheme locally becomes a first-order upstream-differencing scheme. The approach used was adapted from a concept by Mahlman and Moxim (1978). Consider the one-dimensional treatment of the arbitrary field variable ϕ. The Crowley (1968) scheme with explicit mixing is formulated as

$$\phi_i^{\tau+1}=\phi_i^{\tau}-\frac{\Delta t}{\Delta x}(F_{i+\frac{1}{2}}^{\tau}-F_{i-\frac{1}{2}}^{\tau})+\frac{\Delta t}{\Delta x^2}[K_{i+\frac{1}{2}}(\phi_{i+1}^{\tau}-\phi_i^{\tau}) - K_{i-\frac{1}{2}}(\phi_i^{\tau}-\phi_{i-1}^{\tau})], \quad (4.1)$$

where

$$F_{i+\frac{1}{2}}\frac{\Delta t}{\Delta x}=\frac{\alpha_{i+\frac{1}{2}}}{2}(\phi_{i+1}+\phi_i)-\frac{\alpha_{i+\frac{1}{2}}^2}{2}(\phi_{i+1}-\phi_i), \quad (4.2)$$

$$\alpha_{i+\frac{1}{2}}=u_{i+\frac{1}{2}}\frac{\Delta t}{\Delta x}, \quad (4.3)$$

and we let

$$K_{i+\frac{1}{2}}=K_{M_{i+\frac{1}{2}}}+\left|\frac{\alpha_{i+\frac{1}{2}}}{2}\right|(1-|\alpha_{i+\frac{1}{2}}|) \times\frac{\Delta x^2}{\Delta t}\left|\frac{\phi_{i+1}-\phi_i}{\phi_{i+1}+\phi_i-2\phi_0+\Delta_0}\right|^2, \quad (4.4)$$

where ϕ_0 is the threshold value of ϕ and Δ_0 is some small positive parameter $\sim 10^{-10}$. When $\phi_{i+1}>\phi_0$ and $\phi_i=\phi_0$ then (4.1)–(4.4) reduce to an upstream formulation. When $\phi_{i+1}\sim\phi_i$ then the modification rapidly approaches zero. This nonlinear switch does not satisfy the sufficient conditions for a monotone operator as described by Harten (1978) which guarantees positive definiteness. However, the present formulation proved adequate for this application. Maintaining positive definiteness is important in the treatment of N, $N\mu$ and q_1 because logarithms of q_1 are taken when reconstructing the distribution parameters after the advection diffusion step. Hole filling procedures were originally attempted similar to those used by Mahlman and Sinclair (1977) and Clark (1973) but the logic involved turned out to be far too difficult. The main logical difficulty in hole filling is that not only is positive definiteness to be maintained by appropriate adjustments of the grid volume fluxes, but a certain degree of physical compatibility between N, μ and σ must also be maintained during any such adjustment.

5. Dynamic forcing

During every time step of the model calculations kinetic energy is added through a random forcing function. The method used to add kinetic energy was to set up two groups of three-dimensional wavenumbers where each group's magnitude would be near one of the wavenumbers 1 or 2. One member from each group was randomly chosen to make up the two sets of three-dimensional wavenumbers. Phases were randomly chosen in each direction for each wavenumber component. The magnitude was determined such that the total kinetic energy added per time step ΔKE was equal to $-\epsilon\Delta t$. By adding energy at this rate we eventually end up with a dissipation rate near ϵ. When proportioning energy among the wavenumbers we set

$$\Delta \mathrm{KE}_i\alpha|\bar{k}_i|^{-5/3}, \quad (5.1)$$

where i represents the particular wavenumber set index. Lilly (1972) used a similar low-wavenumber space dynamic forcing for studying two-dimensional turbulence. As in his case, we also determine the forcing function in two different ways, a random component as just discussed and a past time-correlated component. In determining the magnitude of the past time-correlated component only the previous time step random component values were considered.

This procedure of dynamic forcing results in larger scale motions cascading down scale to the smallest resolvable grid scales where dissipation is most effective. When the phase relaxation time scale is finite an irreversible coupling exists between the dynamics and thermodynamics and produces horizontal variability of θ^*, q_v and related fields. The reason for such irreversible coupling is that at each point in the horizontal the vertical structure of temperature and water vapor mixing ratio depends on τ_S. τ_S in turn is a function of the local microphysical population. Through this coupling we produce in the limit an infinite set of very slightly different thermodynamic paths. A parcel of air traversing a closed vertical loop will typically not return to the same level with its initial thermodynamic characteristics because of this hysteretic dependence on τ_S. Thus, an internal source for thermodynamic variability exists through the hysteresis effect of τ_S. The main point of this paper is to study the effect of this internal source on the evolving droplet population characteristics.

The working hypothesis of this paper is that there is some representative time scale over which the hysteresis effect is important, e.g., $\sim\tau_S$. Associated with this time scale there will be spatial scales small enough such that

TABLE 1. Description of runs.

Run	CCl (cm^{-3})	$\bar{w}$ ($m\ s^{-1}$)	Grid size resolution (m)
1	2000	2.0	10.0
2	600	1.0	10.0
3	100	0.5	10.0
4	100	0.5	6.667
5	40	0.5	6.667

populations of droplets will combine through local mixing to produce effective population broadening. Considering the above argument we can now point out one of the pitfalls of the random walk type calculations of Warner (1969b) and Bartlett and Jonas (1972). During their calculations the solutions are continually relaxing back to near equilibrium solutions with only a small portion of the time, say $\sim\tau_S$, being in any sense stochastic. Thus, looking at resulting populations and their variability over different realizations $\sim$100 m above cloud after a random walk path from cloud base is possibly equivalent to looking at their variability over different realizations having traveled only the last 1–10 m of their vertical path. To avoid this large-scale reversibility aspect and still retain the Lagrangian parcel framework would possibly require a model as complicated or more so than the current three-dimensional framework.

One experiment with random dynamic forcing was run for a "bulk-physical" case where $S=0$ everywhere in cloud (i.e., equivalent to $\tau_S=0$). The resulting variances of θ^*, q_v and q_l were approximately four orders of magnitude smaller than any of the results with finite τ_S to be presented. This experiment supports the earlier argument about finite τ_S being responsible for an internal source of thermodynamic variability. Even if we locally introduced some horizontal variability of θ^* at one time level it would quickly dissipate out because there is no mechanism for its sustained support.

6. Description of experiments and results

a. Low-resolution experiments

Five experiments were run with a time step taken as 0.5 s for each run. A typical run extended to about three mean advective time scales for the vertical extent of the domain. This appeared sufficient for statistical equilibrium. The distinguishing features of the runs are given below in Table 1, where the two high-resolution experiments to be discussed in Section 6b are also described. In all cases $\epsilon=-100\ cm^2\ s^{-3}$. In qualitative terms we consider Run 1 as continental CCN conditions, Run 3 as maritime CCN conditions and Run 2 as intermediate. Each case was run with and without dynamic forcing. The experiments run without dynamic forcing will be termed laminar.

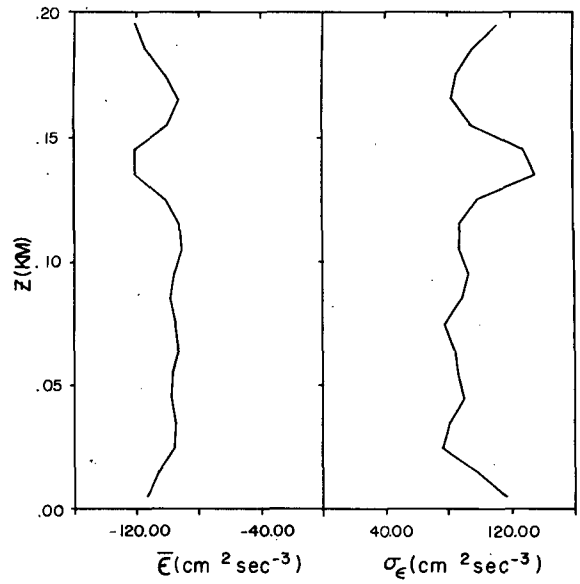

FIG. 2. Dissipation rate profiles ($cm^2\ s^{-3}$) for Run 1. Horizontal means and standard deviations are shown.

At each vertical level, horizontal averages and standard deviations were calculated for various field variables. When displaying vertical profiles of these types of calculations composite averages were calculated where the last five analysis time levels were combined to produce the composite profile. Vertical profiles of $(\overline{u'^2})^{\frac{1}{2}}$, $(\overline{v'^2})^{\frac{1}{2}}$, $(\overline{w'^2})^{\frac{1}{2}}$ will not be shown because they are relatively constant with height and since $\epsilon=-100\ cm^2\ s^{-3}$ for all three runs. Their magnitudes are also relatively constant over the experiments. Typical values

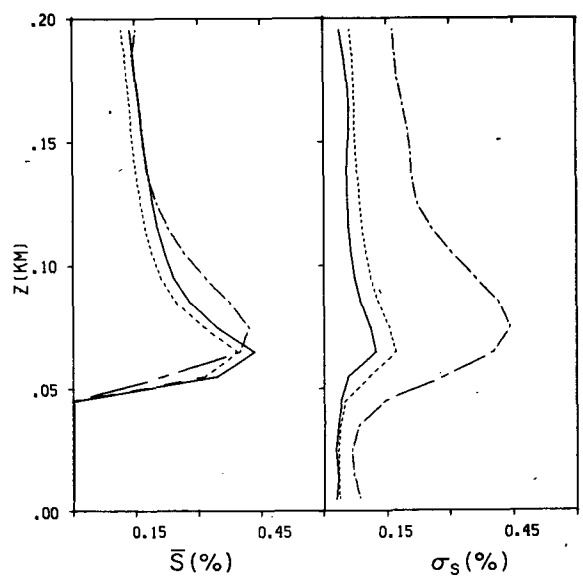

FIG. 3. Supersaturation profiles in units of percent for Runs 1, 2 and 3. Solid line: Run 1, CCl=2000 cm^{-3}, $\bar{w}=2.0\ m\ s^{-1}$; short dashes: Run 2, CCl=600 cm^{-3}, $\bar{w}=1.0\ m\ s^{-1}$; long and short dashes: Run 3, CCl=100 cm^{-3}, $\bar{w}=0.5\ m\ s^{-1}$.

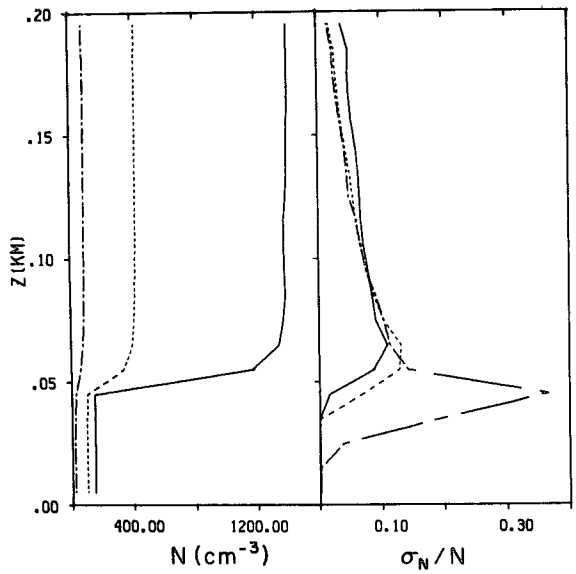

FIG. 4. Number concentration profiles for Runs 1, 2 and 3. The units are in cm^{-3} for the means. The standard deviations are all normalized with respect to their respective means. Same legend as in Fig. 3.

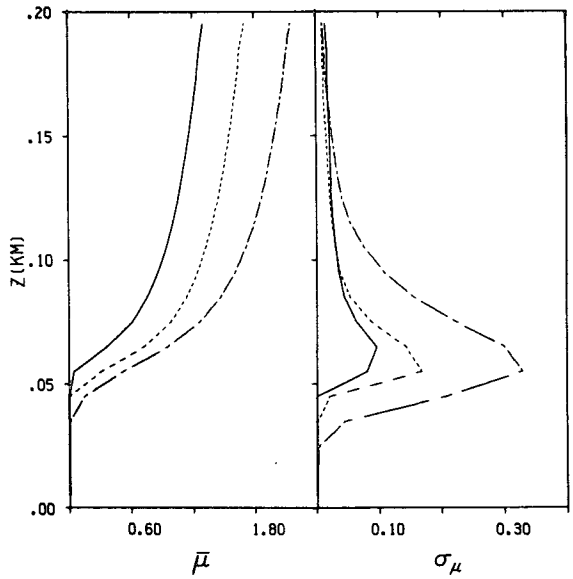

FIG. 6. As in Fig. 3 except for droplet distribution logarithmic mean. Units are normalized with respect to 1 μm.

were $(\overline{u'^2})^{\frac{1}{2}} \approx (\overline{v'^2})^{\frac{1}{2}} \approx 0.466$ m s^{-1} and $(\overline{w'^2})^{\frac{1}{2}} \approx 0.691$ m s^{-1}. The ratio of $w'/u' \sim 1.5$ in the three experiments.

Fig. 2 displays vertical profiles of dissipation rate ϵ for Run 1 which is typical of the five experiments. We see that the standard deviation is typically as large as the mean which is characteristic of the intermittent nature of ϵ.

Figs. 3 to 7 display profiles of supersaturation S; droplet number concentration N; phase relaxation time scale τ_S; droplet logarithmic mean radius μ; and logarithmic standard deviations of the droplet distribution. The coefficient of dispersion μ_d is related to σ through the equation

$$\mu_d = (\overline{R^2}/\bar{R}^2 - 1)^{\frac{1}{2}} = [\exp(\sigma^2) - 1]^{\frac{1}{2}}, \qquad (6.1)$$

so that for values of σ typical in the present experiments $\mu_d \approx \sigma$. We see that $\bar{S}$ profiles are very similar for all three runs due to the choice of CCl and $\bar{w}$. As we progress from Runs 1–3, we see that the magnitudes of $(S'^2)^{\frac{1}{2}}$ clearly increase. Two effects that cause this

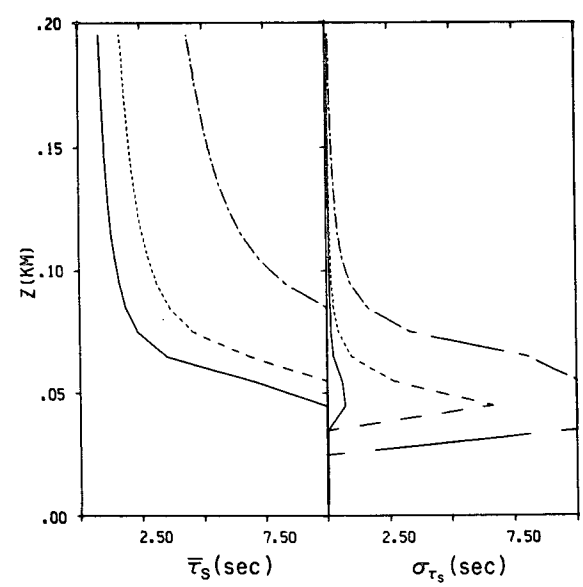

FIG. 5. As in Fig. 3 except for phase relaxation time scale. Units are seconds.

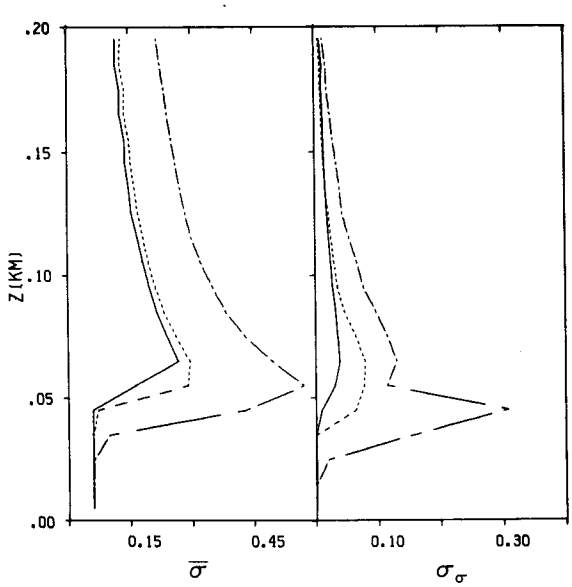

FIG. 7. As in Fig. 3 except for logarithmic standard deviation σ. Units are nondimensional.

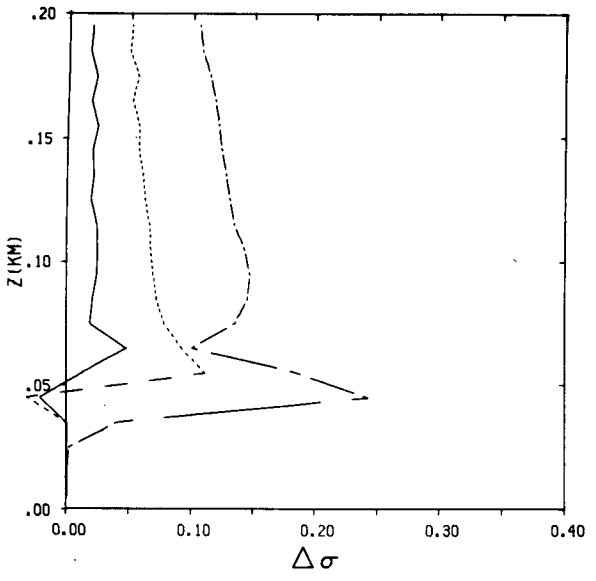

FIG. 8. Vertical profiles of difference between σ from the stochastic experiments and σ from the laminar experiments. Runs 1, 2 and 3 are shown using same legend as in Fig. 3.

increase in horizontal variability of S are (1) the increases in noise to signal ratios $(\overline{w'^2})^{\frac{1}{2}}/\bar{w}$, and (2) the increases in τ_S. Note that in Run 3 the perturbations in S are as large as the means. In Fig. 4 the profiles of N for Runs 1, 2 and 3 are shown. We see that the mean number concentrations level off at approximately 1400, 423 and 93 for Runs 1, 2 and 3, respectively. The standard deviations are all normalized with respect to their means, i.e., represented as coefficients of dispersion. Two aspects of this plot are apparent. First, we see that the relative horizontal variability in N remains unchanged among the three runs, except at the very initial nucleation region. Second, we see a gradual decay of $(\overline{N'^2})^{\frac{1}{2}}/\bar{N}$ with height above the nucleation region. This result is consistent with gradual decay of the horizontal variability away from the source region. Note that there is a slightly less rapid decay rate for Run 3 because $w'/\bar{w}\sim 1$ and there is an increased probability for evaporation and renucleation above the initial cloud base nucleation region. In Fig. 5 profiles of τ_S are displayed for Runs 1, 2 and 3. The mean values of τ_S at $z\sim 200$ m (i.e., 150 m above cloud base) are 0.85, 1.60, and 4.3 s, respectively. Large values of τ_S imply near dry adiabatic ascent and/or descent due to the slow response of the droplet populations to changing humidity conditions. It is only in regions where τ_S is large, or where the effect of the droplet population is very weak, that significant horizontal variations in τ_S occur. At more than 50 m above cloud base the variability of τ_S in the horizontal is extremely small. This is likely due to the strong feedback effects operative in generating $N\bar{R}(\alpha 1/\tau_S)$. Even the relatively strong perturbation forces in Run 3 are not sufficient to cause significant deviations from the mean. Fig. 6 displays profiles of μ for Runs 1, 2 and 3. These profiles are intended primarily for describing the relative variation in logarithmic means among the three runs. As with the profiles of N, we see that above the initial cloud base nucleation region the horizontal deviations become nearly equal for all runs. In this case, though, we do not detect any gradual decay because there is still a source term operative through variations in S'. Fig. 7 displays profiles of σ for Runs 1, 2 and 3 where, as discussed earlier, σ is approximately equal to the coefficient of dispersion for the droplet distribution. The mean values of σ as well as the standard deviation values increase significantly from Run 1 to Run 3. The increasing values of τ_S and/or the increasing ratio $w'/\bar{w}$ seem the likely candidates for producing this effect. A sufficient number of experiments have not been carried out to properly isolate the functional response to τ_S and τ_L. It is encouraging to see that for Run 3 the mean values of σ predicted are in the range of values observed by Warner (1969a).

The profile of σ shown in Fig. 7 are difficult to interpret because of possible effects of numerical procedures. In order to isolate such effects, laminar cases were run without any dynamic forcing present for each of the three runs. The difference between mean σ of the stochastic runs and mean σ of the laminar runs is shown in Fig. 8. We see a rather strong increase of $\Delta\sigma$ from Runs 1 to 3 which suggests that the mean values presented in Fig. 7 were due to differences in the physical regime.

Correlation coefficients were calculated at each horizontal level for various parameter pairs. It was found that the correlation coefficient between potential temperature and water vapor mixing ratio C_{θ,q_v} steadied out to -1 at all levels. For layers as shallow as 200 m

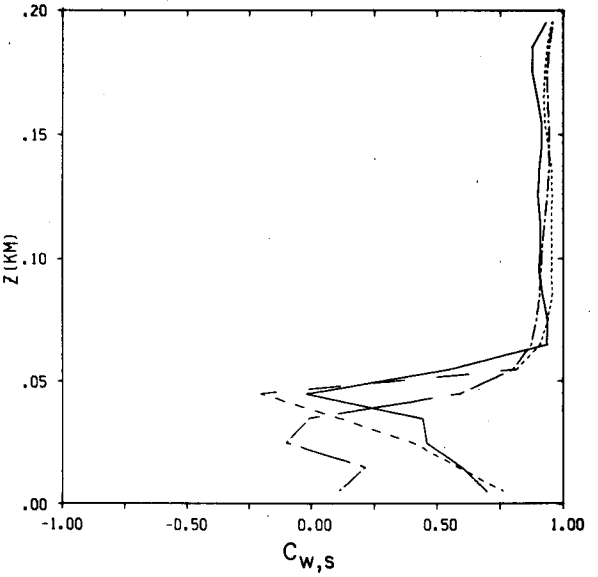

FIG. 9. Vertical profiles of correlation coefficients between w and S for Runs 1, 2 and 3. Legend is same as in Fig. 3.

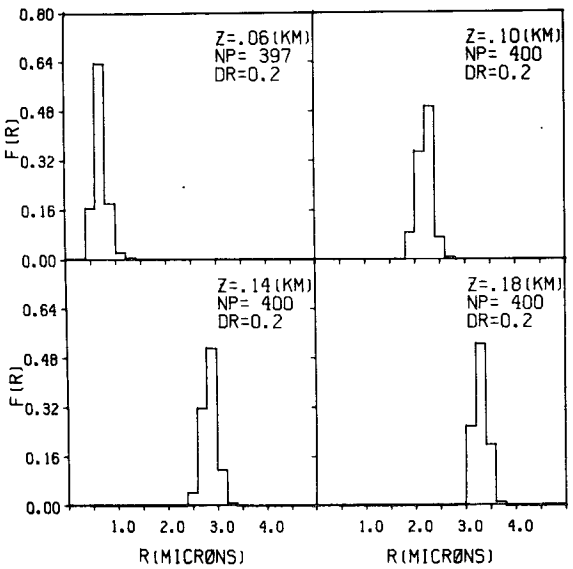

FIG. 10. Distribution functions at four different height levels derived from a Lagrangian particle experiment. The spatial extent of sampling is over the full 200 m×200 m horizontal domain. The total number of particles used to produce the plot is shown in the upper right-hand corner along with radii interval. This figure is for Run 1.

relative changes in potential temperature and temperature are nearly equivalent and theoretical considerations strongly suggest that -1 is the correct value for C_{θ,q_v}. Fig. 9 displays profiles of $C_{w,s}$ for Runs 1, 2 and 3. We see that the correlation between w and S is very strong for all three experiments where $C_{w,s}\sim 0.95$. This high level of positive correlation between S and w over such a large range of physical and dynamical parameters as τ_S and $w'/\bar{w}$ suggests that the numerical

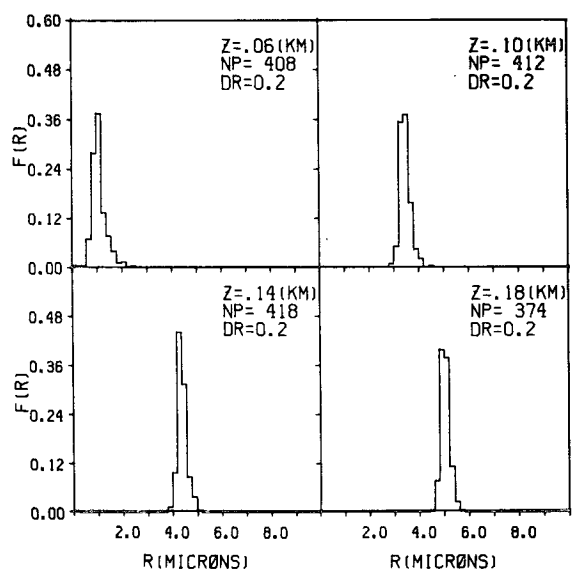

FIG. 11. As in Fig. 10 except for Run 2.

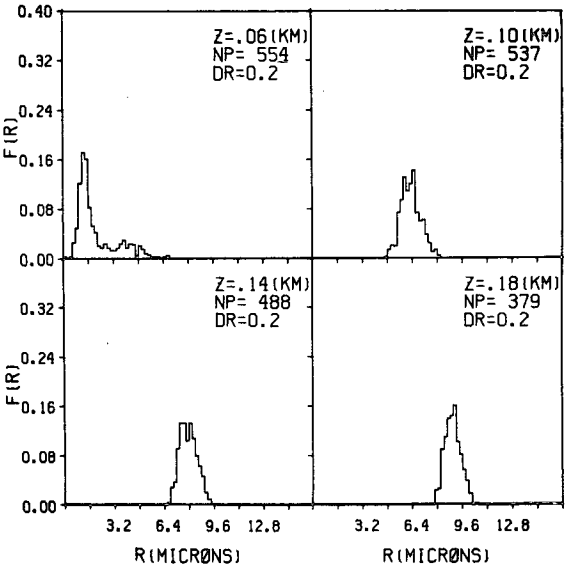

FIG. 12. As in Fig. 10 except for Run 3.

resolution may be too low to properly capture any differences.

Figs. 10, 11 and 12 display density function structures at various vertical levels for the Lagrangian particle experiments in Runs 1, 2 and 3, respectively. In each of these figures the amplitude of $f(r)$ is normalized by dividing the number of particles in the 0.2 μm interval by the total number of particles NP. We see that as we progress from Runs 1–3 the normalized amplitudes significantly decrease, indicating increased dispersion. For any one run the maximum amplitude remains approximately constant which is again an indication

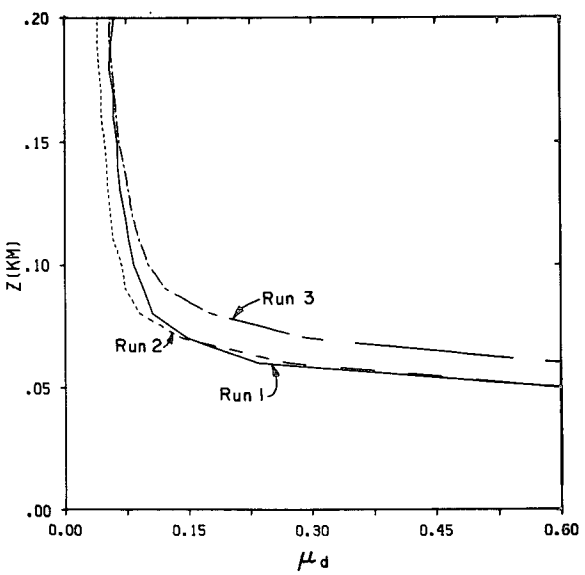

FIG. 13. Profiles of coefficient of dispersion μ_d for Runs 1, 2 and 3 Lagrangian particle experiments.

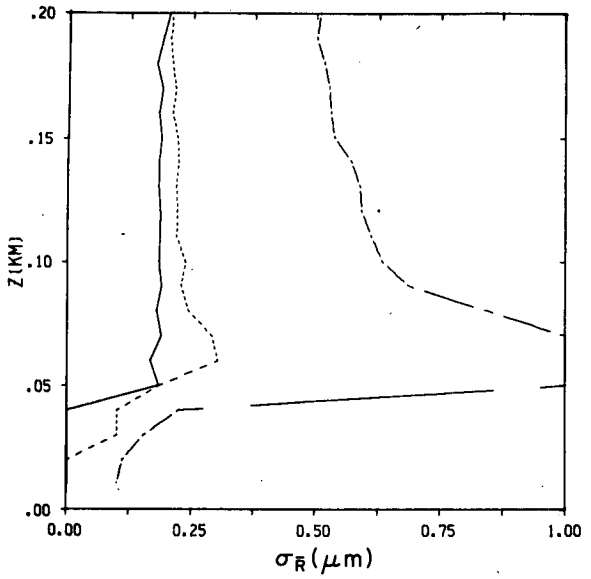

FIG. 14. Profiles of standard deviation of the droplet population radii for Runs 1, 2 and 3 Lagrangian particle experiments.

of dispersive effects because laminar theory would result in a strong increase in maximum amplitude with height for any initial distribution of finite breadth. At 10 m above cloud base in Run 3, Fig. 12, we see a bimodal distribution, whereas at higher levels we see only monomodal distributions.

Fig. 13 displays $\mu_d(z)$ for the Lagrangian particle experiments. In the upper levels above cloud base we see that μ_d is only about half the values shown in Fig. 8. Since the Lagrangian experiments supposedly represent a lower bound calculation of μ_d we might assume that the actual physical effect on distribution broadening lies somewhere between Figs. 8 and 13. Fig. 14 displays the standard deviation of radius with height for Runs 1, 2 and 3. We see a slight increase from Runs 1–2 and a much larger increase from 2–3.

b. *High-resolution experiments*

These experiments were run with a grid scale of 6.667 m in the three spatial directions. In the first high-resolution experiment, except for spatial resolution, all other parameters and initial conditions were identical to Run 3. The purpose of this experiment was to test the effect of grid resolution on the previous results. It should be stressed that the effective resolution increase in resolving the actual physical coupling effects between the microphysics and thermodynamics is minimal. To actually get better resolution in this direction we feel that L_S would have to be dramatically increased by going to very low number concentrations and/or going to much larger dissipation rates. The main advantage of going to the higher resolution is that the spatial separation between the dynamically forced scales and the smallest resolved scales is effectively increased.

A comparison between the profiles of the present experiment, subsequently termed Run 4, and Run 3 showed little significant change. The main comparisons will be confined to the Lagrangian particle experiments. Fig. 15 shows a comparison of μ_d profiles between Runs 3 and 4. We see that for $z>100$ m, μ_d is slightly less for Run 4 and for $z<100$ m, μ_d is slightly larger for Run 4. Even though the differences are too small to be seriously stressed, it is encouraging to see μ_d larger in the lower levels where the grid scales are better able to resolve scales $\sim L_S$. The overall differences could easily be attributed to either the increased number of particles; or better resolution for the smaller eddies coupled with upper boundary effects. The comparison

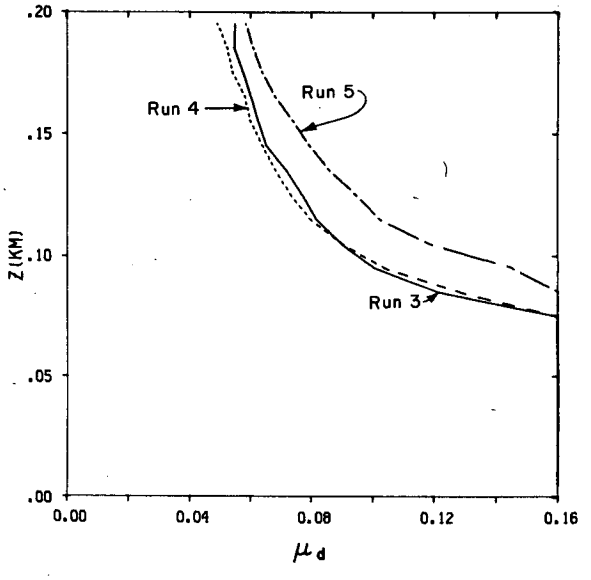

FIG. 15. Comparison of μ_d between Run 3, Run 4 and Run 5.

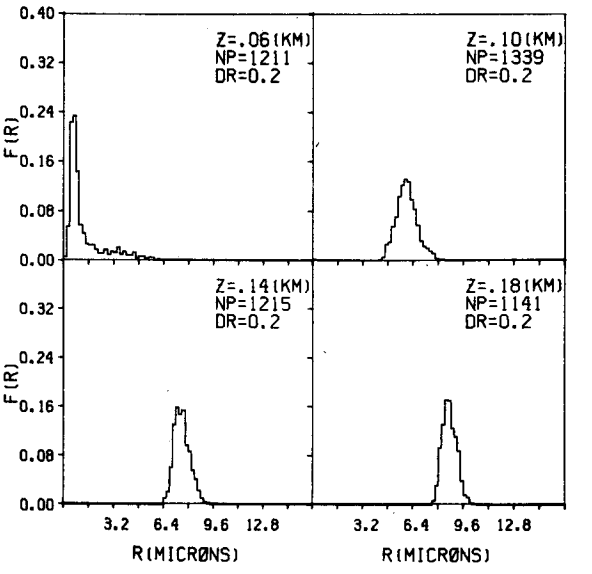

FIG. 16. As in Fig. 10 except for Run 4.

between Runs 3 and 4 does strongly suggest that the earlier discussed results are maintained with increased resolution.

Fig. 16 shows the Lagrangian particle distributions at four height levels. A comparison with Fig. 12 shows many of the same characteristics with a slight increase in maximum values for Run 4. The bimodal structure in the lowest level is somewhat less pronounced in Run 4 than in Run 3.

The effect of increasing τ_S is emphasized in Run 5 where CCI has been reduced from 100–40 cm^{-3}. As shown in Table 1, all other aspects of Run 5 are identical to Run 4. Fig. 17 shows the Lagrangian particle distributions at four height levels. We still have a strongly skewed-type distribution at 10 m above cloud base with much stronger dispersion at all heights compared to earlier runs. For reference $\mu_d(z)$ is shown in Fig. 15 for Runs 3, 4 and 5. A comparison of Figs. 17 and 16 shows a significant increase in dispersion with height from Run 4 and the peak values of $f(r)$ in Fig. 17 are reduced as a consequence of this increased dispersion. Fig. 18 shows the correlation coefficient $C_{w,S}$ for Runs 4 and 5. We see a relatively small but systematic reduction in $C_{w,S}$ from Runs 4 to 5.

In changing the CCl parameter from 100–40 we have changed L_S by approximately a factor of 2. The increased dispersion is then likely due to two factors: first, increasing τ_S is certain to increase irreversible coupling effects for any specific spatial scale; and secondly, the grid resolution has doubled in terms of L_S so that more of the spatial scales involved in this coupling can be resolved. Unfortunately, we have not yet been able to delineate these two effects.

Fig. 19 shows a typical snapshot of w', θ'', q_v'' and S'' from Run 4. These are vertical cross-sections with y=constant taken through the middle of the domain.

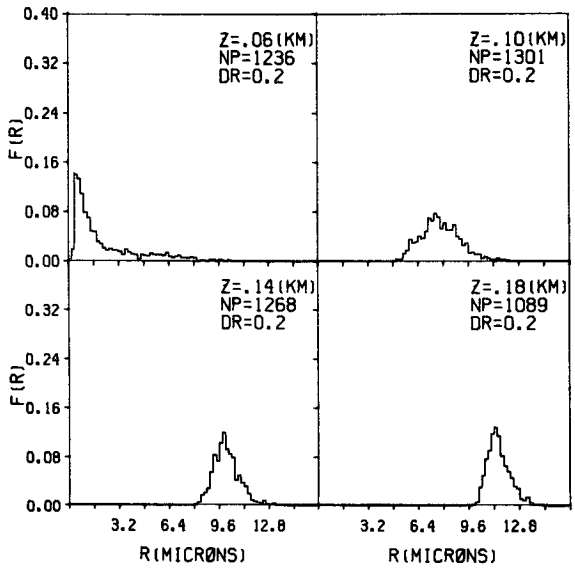

FIG. 17. As in Fig. 10 except for Run 5.

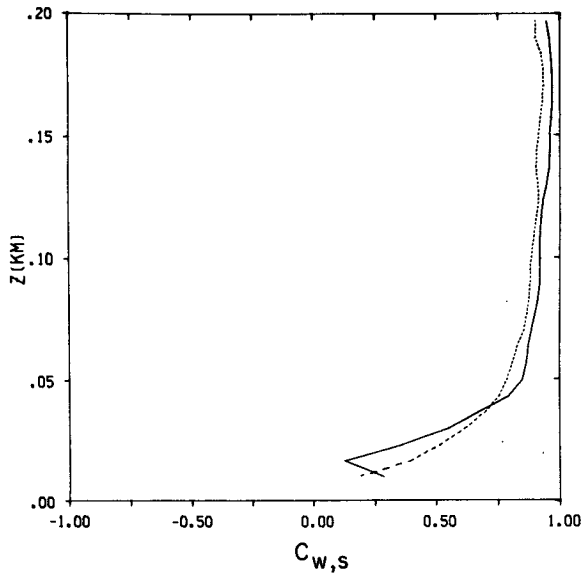

FIG. 18. As in Fig. 9 except for Run 4 (solid line) and Run 5 (dashed line).

The strong correlations between all the fields and w' are visually evident. The strong S'' perturbations are primarily due to θ'' because of the exponential nature of q_{v_s}, but it is interesting to note that the positive q_v'' perturbations constructively combine with the negative θ'' perturbations in producing S''.

7. Conclusions

Two types of numerical calculations were performed to assess the importance of the irreversible coupling between the cloud physics and the thermodynamics on the evolving droplet population. The first type was a totally Eulerian-type calculation with parameterized cloud physics and the second was an embedded Lagrangian particle experiment which was run in parallel with the Eulerian model. The results from the Eulerian model showed that significant horizontal variations in all of the thermodynamic and microphysical fields resulted from the irreversible coupling caused by finite values of the phase relaxation time scale τ_S. The amplitudes of variations increased with increasing τ_S as well as with increasing Lagrangian time scale τ_L. In three experiments, Runs 3, 4 and 5, the standard deviation of the supersaturation in the x-y plane was as large as or larger than the horizontally-averaged mean values. The coefficients of dispersion for the droplet populations in the upper levels above cloud base increased with decreasing number concentration such that for a maritime CCN case $\mu_d \sim 0.10$ above the laminar case were found. In the experiments presented the irreversible coupling effect introduced by finite values of τ_S failed to produce increasing μ_d with height as observed by Warner (1969a).

The Lagrangian particle experiments resulted in

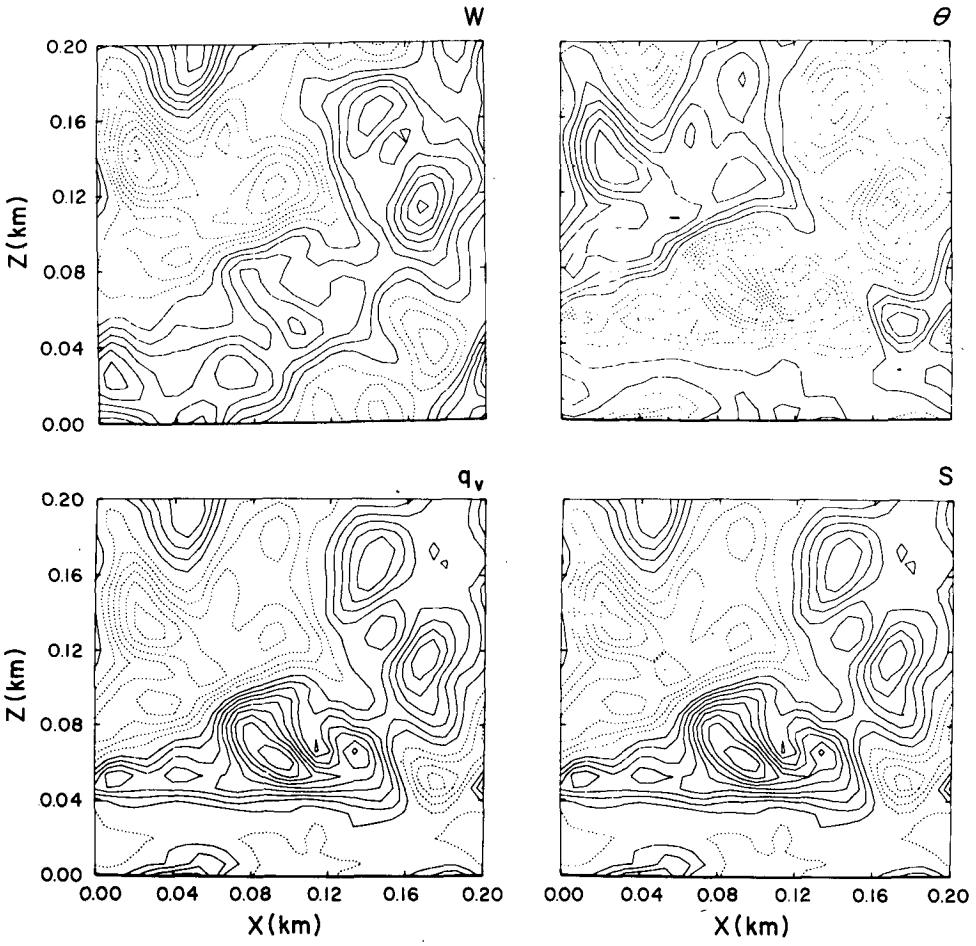

FIG. 19. Field plots of w', θ'', q_v'' and S'' at $t=780$ s for Run 4. Contour interval for field are 0.22 m s^{-1}, 0.006 K, 0.002 g kg^{-1} and 0.07% for w', θ'', q_v'' and S'', respectively. Dashed region indicates negative field values.

profiles of μ_d about one-half the values of the Eulerian experiments, but as stressed in the text, these results are more representative of a lower bound type calculation because influences such as the finite time scale of nucleation are ignored. The structural characteristics of the spectral plots from the Lagrangian particle experiments showed either a bimodal or strongly skewed character in the regions close to cloud base for the most maritime case, whereas at all upper levels a monomodal distribution resulted. We were not able to produce increasing values of population dispersion with height.

The present set of experiments has shown that the irreversible coupling caused by finite values of τ_S can produce significant small-scale variability in the horizontal. This is particularly the case for the supersaturation. It should be remembered that other source terms such as the downgradient flux of thermodynamic variability have been purposely neglected. Inclusion of such effects would likely increase the magnitude of these small-scale fluctuations as well as possibly increase their population dispersion effectiveness through reduced correlation coefficients with w.

The results from the present set of experiments should be considered as preliminary because of certain deficiencies. Since physically realistic values of ϵ and CCN concentration were chosen, it was not possible to properly resolve the very small-scale interactions caused by τ_S and still maintain a cloud depth $\sim$150 m. In order to better resolve the actual scales of interaction it seems necessary to either use unrealistically low number concentrations and/or very large values of ϵ. Such experiments, a more detailed analysis and comparison with observations will be considered in the future.

Acknowledgments. One of the authors (W.D.H.) wishes to acknowledge the support received by the Advance Study Program at NCAR while doing this research.

REFERENCES

Arakawa, A., 1966: Computational design for long-term numerical integration of the equations of fluid motion: Two-dimensional incompressible flow. Part I. *J. Comput. Phys.*, 1, 119–143.

Arnason, G., and R. S. Greenfield, 1972: Micro- and macro-

structures of numerically simulated convective clouds. *J. Atmos. Sci.*, **29**, 342–367.

Bartlett, J. T., and P. R. Jonas, 1972: On the dispersion of the sizes of droplets growing by condensation in turbulent clouds. *Quart. J. Roy. Meteor. Soc.*, **98**, 150–164.

Belyaev, V. I., 1967: The evolution of the droplet condensation spectrum in clouds. *Izv. Atmos. Ocean. Phys.*, **3**, 341–343.

Chodes, N., J. Warner and A. Gagin, 1974: A determination of the condensation coefficient of water from the growth rate of small cloud droplets. *J. Atmos. Sci.*, **31**, 1351–1357.

Clark, Terry L., 1973: Numerical modeling of the dynamics and microphysics of warm cumulus convection. *J. Atmos. Sci.*, **30**, 857–878.

——, 1974a: On modeling nucleation and condensation theory in Eulerian spatial domain. *J. Atmos. Sci.*, **31**, 2099–2117.

——, 1974b: A study in cloud phase parameterization using the gamma distribution. *J. Atmos. Sci.*, **31**, 142–155.

——, 1977: A small-scale dynamic model using a terrain-following coordinate transformation. *J. Comput. Phys.*, **24**, 186–215.

——, 1979: Further developments in warm rain microphysical parameterizations using lognormal distribution functions. *J. Atmos. Sci.*, **36** (in press).

Crowley, W. P., 1968: Numerical advection experiments. *Mon. Wea. Rev.*, **96**, 1–11.

Deardorff, J. W., 1971: On the magnitude of the subgrid scale eddy coefficient. *J. Comput. Phys.*, **7**, 120–133.

Harten, A., 1978: The artificial compression method for computation of shocks and contact discontinuities: III: Self-adjusting hybrid schemes. *Math. Comput.*, **32**, 363–389.

Howell, W. E., 1949: The growth of cloud drops in uniformly cooled air. *J. Meteor.*, **6**, 134–149.

Kabanov, A. S., I. P. Mazin and V. I. Smirnov, 1971: Comments on "The Theory of growth of cloud drops by condensation." *J. Atmos. Sci.*, **28**, 129–130.

Lilly, D. K., 1962: On the numerical simulation of buoyant convection. *Tellus*, **14**, 148–172.

——, 1972: Numerical simulation studies of two-dimensional turbulence. *Geophys. Fluid Dyn.*, **3**, 289–319.

Mahlman, J. D., and R. W. Sinclair, 1977: Tests of various numerical algorithms applied to a simple trace constituent air transport problem. *Fate of Pollutants in the Air and Water Environments*, Part I, Vol. 8, *Advances in Environmental Science and Technology*, I. H. Suffet, Ed., Wiley, 223–252.

——, and W. J. Moxim, 1978: Tracer simulation using a global general circulation model: Results from a mid-latitude instantaneous source experiment. *J. Atmos. Sci.*, **35**, 1340–1374.

MacPherson, J. I., and G. A. Isaac, 1977: Turbulent characteristics of some Canadian cumulus clouds. *J. Appl. Meteor.*, **16**, 81–90.

Mordy, W., 1959: Computations of the growth by condensation of a population of cloud droplets. *Tellus*, **11**, 16–44.

Neiburger, M., and C. W. Chien, 1960: Computations of the growth of cloud drops by condensation using an electronic digital computer. *Physics of Precipitation, Geophys. Monogr.*, No. 5, Amer. Geophys. Union, 191–210.

Ogura, Y., and N. A. Phillips, 1962: Scale analysis of deep and shallow convection in the atmosphere. *J. Atmos. Sci.*, **19**, 173–179.

Sedunov, Y. S., 1965: Fine cloud structure and its role in the formation of the cloud particle spectrum. *Izv. Atmos. Ocean. Phys.*, **1**, 722–731.

Smagorinsky, J., 1963: General circulation experiments with the primitive equations: 1. The basic experiment. *Mon. Wea. Rev.*, **91**, 99–164.

Soong, Su-Tzai, 1974: Numerical simulation of warm rain development in an axisymmetric cloud model. *J. Atmos. Sci.*, **31**, 1262–1285.

Squires, P., 1952: The growth of cloud drops by condensation. *Aust. J. Sci. Res.*, **A5**, 59–86.

Stepanov, A. S., 1975: Condensational growth of cloud drops in a turbulized atmosphere. *Izv. Atmos. Ocean. Phys.*, **11**, 27–42.

Takeda, T., 1971: Numerical simulation of a precipitating convective cloud: The formation of a "long-lasting" cloud. *J. Atmos. Sci.*, **28**, 350–376.

Warner, J., 1969a: The microstructure of cumulus clouds. Part I. General features of the droplet spectrum. *J. Atmos. Sci.*, **26**, 1049–1059.

——, 1969b: The microstructure of cumulus clouds. Part II: The effect on droplet size distribution of the cloud nucleus spectrum and updraft velocity. *J. Atmos. Sci.*, **26**, 1272–1282.